Tissue Characterization of Equine Tendons With Clinical B-Scan Images Using a Shock Filter Thinning Algorithm

4 authors, including:

Ali Meghoufel
Université du Québec à Montréal
7 PUBLICATIONS   **19** CITATIONS

SEE PROFILE

Nathalie Crevier-Denoix
École Nationale Vétérinaire d'Alfort
81 PUBLICATIONS   **624** CITATIONS

SEE PROFILE

Jacques A de Guise
École de Technologie Supérieure
356 PUBLICATIONS   **5,949** CITATIONS

SEE PROFILE

Some of the authors of this publication are also working on these related projects:

Project Improvements in 3D knee kinematics variability using functional principle component analysis after anterior cruciate ligament reconstructive surgery in adolescence View project

Project Peripheral Arterial Diseases View project

Tissue Characterization of Equine Tendons With Clinical *B*-Scan Images Using a Shock Filter Thinning Algorithm

Ali Meghoufel*, Guy Cloutier, Nathalie Crevier-Denoix, and Jacques A. de Guise

Abstract—The fiber bundle density (FBD) calculated from ultrasound *B*-scan images of the equine superficial digital flexor tendon (SDFT) can serve as an objective measurement to characterize the three metacarpal sites of normal SDFTs, and also to discriminate a healthy SDFT from an injured one. In this paper, we propose a shock filter algorithm for the thinning of hyper-echoic structures observed in *B*-scan images of the SDFT. This algorithm is further enhanced by applying closing morphological operations on filtered images to facilitate extraction and quantification of fiber bundle fascicles. The mean FBD values were calculated from a clinical *B*-scan image dataset of eight normal and five injured SDFTs. The FBD values measured at three different tendon sites in normal cases show a highest density on the proximal site (five cases out of eight) and a lowest value on the distal part (seven cases out of eight). The mean FBD values measured on the entire tendon from the whole *B*-scan image dataset show a significant difference between normal and injured SDFTs: 51 (±9) for the normal SDFTs and 39 (±7) for the injured ones ($p = 0.004$). This difference likely indicates disruption of some fiber fascicle bundles where lesions occurred. To conclude, the potential of this imaging technique is shown to be efficient for anatomical structural SDFT characterizations, and opens the way to clinically identifying the integrity of SDFTs.

Index Terms—*B*-scan images, equine tendon, fiber bundle density, mathematical morphological operations, shock filter, thinning algorithm, two-dimensional/three-dimensional (2D/3D) anatomical structures, ultrasound imaging.

I. INTRODUCTION

ULTRASOUND (US) imaging is a noninvasive diagnostic tool used to evaluate equine superficial digital flexor tendon (SDFT) structures after injury and during the healing process [1]. This technique is routinely used in everyday veterinary practice for diagnostic purposes, for the serial assessment of lesion healing, and for the evaluation of treatments. With the help of a medical US scanner, clinicians can qualitatively and subjectively evaluate tendon integrity or disruption; however they still do not have a tool for objectively quantifying the full internal structures or to offer an accurate prognosis for recovery.

The SDFT consists of highly specialized connective tissues organized into a hierarchy of structures which include collagen (the main structural protein), fibrils, fibers, and fascicles [2]–[4]. As shown in Fig. 1(a), the fibers are arranged in primary fiber bundles that are gathered together to form secondary fiber bundles (fascicles), which are in turn joined together to form tertiary fiber bundles. Fiber fascicle bundles are surrounded by loose connective tissue, called the interfascicular space, which provides vascular supply, lymphatic vessels, and probably a circular mechanical support. The fascicles are regularly parallel to the SDFT loading axis.

Three preferential sites are usually chosen on the SDFT to evaluate fiber bundle density (FBD) [5]: the proximal, middle, and distal regions [see Fig. 1(b)]. The proximal metacarpal site describes the point of attachment of the tendon to the upper part of the horse's leg and has an approximately circular cross sectional area (CSA). The distal metacarpal site describes the point of attachment of the tendon to the lower part of the horse's leg, and has a thin, flattened, crescent-shaped CSA. The central part of the tendon (middle) has an elliptical CSA. The proximal, middle, and distal sites occupy 25%, 50%, and 25% of the total length of the tendon, respectively.

The main diagnostic criterion for assessing the integrity of the SDFT is the *B*-scan image echogenicity [6], [7]. The echogenicity feature of a normal SDFT is the presence of parallel and linear hyper-echoic structures caused by coherent specular reflections at the interfascicular spaces [8], when scanning is performed by aligning such structures perpendicularly to the US beam [Fig. 2(a) and (b)]. In the case of a lesion [Fig. 2(c) and (d)], some disorganization of the interfascicular spaces and loss in collagen density occur, resulting in a reduction in echogenicity [5].

The internal structure analysis of the tendon is very dependent on what veterinarians observe on the *B*-scans. Therefore, the analysis of the integrity of the tendon is subjective. To improve diagnosis based on the postprocessing of acquired images, veterinarians would benefit from an imaging tool able to identify automatically the structures of the tendon without recourse to the human eye. To do this, we propose the use of an original

*A. Meghoufel is with the Département du génie de la production automatisée, École de Technologie Supérieure, University of Québec in Montreal, Montréal, QC, H3C 1K3 Canada (e-mail: ali.meghoufel@etsmtl.ca).

G. Cloutier is with the Laboratoire de biorhéologie et d'ultrasonographie médicale, University of Montreal Hospital (CRCHUM), Montréal, QC, H2L 2W5 Canada; and with de Department of Radiology, Radio-Oncology and Nuclear Medicine, and Institute of Biomedical Engineering, University of Montreal, Montréal, QC, H3T 1J4 Canada (e-mail: guy.cloutier@umontreal.ca).

N. Crevier-Denoix is with the Unité INRA-ENVA de Biomécanique et Pathologie Locomotrice du Cheval, École Nationale Vétérinaire d'Alfort, Maisons-Alfort 94704, France (e-mail: ncrevier@vet-alfort.fr).

J. A. de Guise is with the Laboratoire de recherche en imagerie et orthopédie, University of Montreal Hospital (CRCHUM), Montréal, QC, H2L 2W5 Canada; and with the Département du génie de la production automatisée, École de Technologie Supérieure, University of Québec in Montreal, Montréal, QC, H3C 1K3 Canada (e-mail: jacques.deguise@etsmtl.ca).
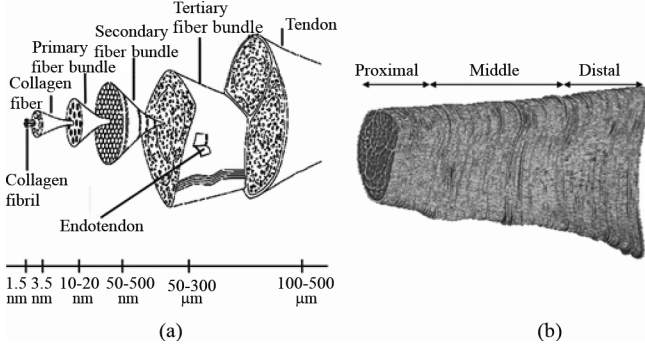
Fig. 1. (a) Hierarchical organization of the tendon [2] and (b) three metacarpal sites of the SDFT.
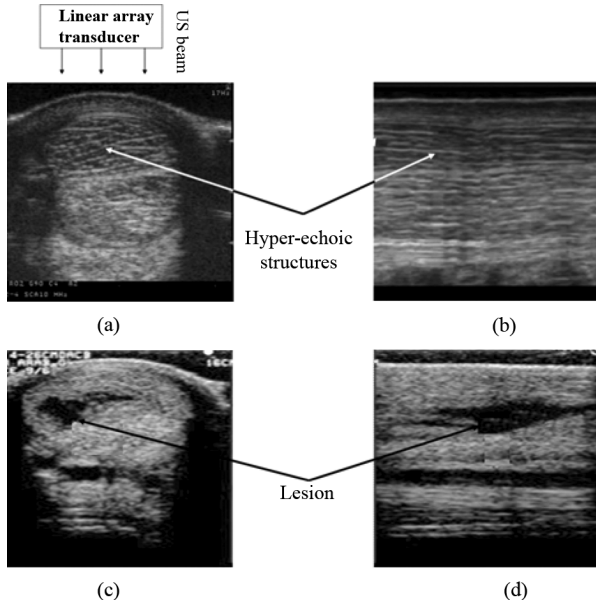

Fig. 2. 2D *B*-scan images of metacarpal SDFTs. Cross sectional and longitudinal views of a normal SDFT, (a) and (b), and of an injured SDFT, (c) and (d).

imaging technique that allows extracting accurately the internal structure of the tendon. The next paragraphs focus on the state of the art of imaging techniques applied to SDFT *B*-scan images, and on the proposed technique and its mathematical foundation.

SDFT *B*-scan image processing requires several stages, first the SDFT integrity assessment that was limited to content quantification by texture analysis and first-order grey-level representation [9]–[11]. These studies have often led to conflicting results on the sources of the observed hyper-echoic structures of the *B*-scans and on discriminating normal from injured tendon [10]. Qualitative *B*-scan image analysis revealed that the hyper-echoic structure density observed on the CSA *B*-scan image planes decreases from the proximal to the distal metacarpal sites [7], [12], which likely indicates less FBD in the distal region. Such results (less FBD) may signify mechanical weaknesses in traction and consequently explain the high occurrence of lesions at this site [5], [13]. Recently, more robust imaging techniques have been designed in order to understand accurately the content of those images: among them, the spectral analysis of SDFT echo signal has been proposed [12]. In this study, the authors have described mathematical simulation models to clarify

the relationship between the backscattering and structure thicknesses and also to correlate the echo spectra with high-resolution images from several modalities; authors conclude that the interfascicular space thicknesses and their ionization angle are predominant factors explaining hyper-echoic structures. The last study conducted by us [8] proposed an original imaging technique based on simulations of *B*-scan images revealing that the interfascicular spaces are most likely responsible for hyper-echoic structures on *B*-scan images; and discrimination between normal and injured *B*-scan images of SDFT.

Beside information on echogenicity density, it would be relevant to quantitatively assess the structural integrity of tendons and the extent of healing to support the decision as to whether or not a horse can resume training and racing, and if so when. To do this, the extraction of the interfascicular spaces corresponding to the intact fiber bundle fascicles by an appropriate segmentation method meets perfectly this goal.

Among segmentation methods in the literature that relate to our problem are variational methods and specifically shock filters. A shock filter is a nonlinear hyperbolic partial differential equation (PDE) filter [14]–[17] regarded as a deconvolution filter used to segment an image on piecewise constant segmentations. Inspired by the existing deconvolution shock filter algorithms, we present an alternative approach that allows the thinning (rather than the deconvolution) of the observed hyper-echoic structures corresponding to the interfascicular spaces [8] to facilitate their extraction. The algorithm is based on the analytical shock filter form described in [14] and on the numerical scheme developed in [18], adapted to handle *B*-scan images. Closing morphological operations are subsequently applied to the enhanced images.

The proposed thinning algorithm is presented first analytically and numerically in the 1D case to clarify its behaviour and to compare it with the classical deconvolution algorithm, then the 2D algorithm is applied to ultrasound images. The morphological operations are used in the final step to characterize fiber fascicle bundles as binary closed structures. The quantification of the FBD allowed the discrimination between normal and injured SDFTs. It was also used to explain the mechanical strength properties of the metacarpal in traction, and the frequent appearance of lesions in its distal site [13].

II. PREVIOUS SHOCK FILTER MODELS

Shock filter algorithms rely on image deconvolution to create sharp discontinuities (the "shocks") between adjacent grey-scale zones (influence zones) in the images and produce piecewise constant segmentations. The concept of image shock filter enhancement is adapted from nonlinear hyperbolic techniques [17]. In the following equations, the u denotes the 1D signal and the I denotes the 2D signal or the *B*-scan image. In the 1D case, the signal $u(x,t)$ verifies the following hyperbolic equation:

$$u_t = a \cdot u_x \tag{1}$$

with the initial signal $u(x, t = 0) = u^0$, and the scalar $a \geq 0$. u_t and u_x are the first derivatives in time and in space respectively.
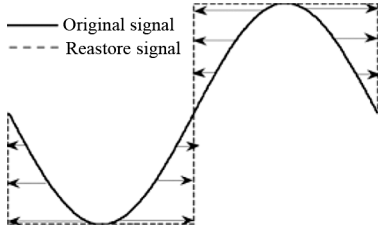
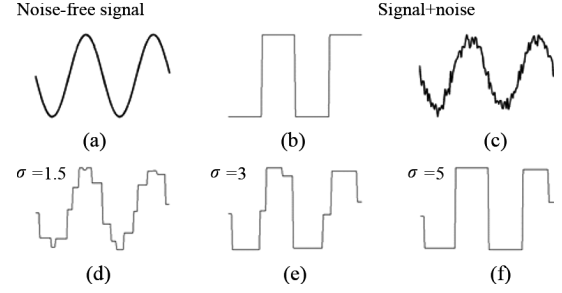Fig. 3. Piece-wise segmentation of a curved noise-free 1D signal.

Fig. 4. 1D shock deconvolution process of (5) with various Gaussian smoothing kernels σ. Top row (from left): (a) original noise-free signal (sine wave), (b) noise-free signal restored by the shock filter, (c) original signal + white *Gaussian* noise defined with a $\mathrm{SNR} = 10$; bottom: noised signal restored using Gaussian deblurring, (d) with $\sigma = 1.5$, (e) $\sigma = 3$, and (f) $\sigma = 5$.

The solution of (1) is $u(x, t) = u^0(x + at)$, and it corresponds to the initial signal propagated at speed $-a$.

In order to integrate signal deblurring and enhancement into the previous 1D model of (1), it was suggested to force the signal propagation speed to depend on the signal itself [15], [16], and, more precisely on the *sign* of the second spatial derivative u_{xx}. This suggestion led Osher and Rudin [16], [17] to propose their 1D model, which is written as follows:

$$u_t = -sign\,(u_{xx})\,|u_x|. \tag{2}$$

This model of (2) can be interpreted as mathematical morphological operations [19]. Indeed, according to the *sign* of the second derivative u_{xx}, (2) can be decomposed into three parts, as follows:

$$u_t = \begin{cases} |u_x| & u_{xx} < 0 \\ -|u_x| & u_{xx} > 0 \\ 0 & u_{xx} = 0. \end{cases} \tag{3}$$

Shocks occur at signal inflection points (zero-crossings of u_{xx}) and lead to piece-wise constant solutions. As shown in Fig. 3, the shock process performs dilatation by solving $u_t = |u_x|$ in concave signal segments, whereas, in convex segments, measurement of the erosion that takes place is achieved by solving $u_t = -|u_x|$. The shock process maintains local extrema (maxima and minima) constant in time, without creating new ones.

The 2D shock filter model of Osher and Rudin [16], [17] has the following form:

$$I_t = -F\,(I_{\eta\eta})\,|\nabla I| \tag{4}$$

with the initial condition (original image) $I(x, y, t = 0) = I^0$, the gradient direction $\eta = \nabla I / \|\nabla I\|$, and the 2D shock function F, which must satisfies $F(0,0) = (0,0)$, and $(x, y) \times F(x, y) \geq 0$. $F(x, y) = (sign(x), sign(y))$ was chosen in [16], [17] to be the shock function in the case of (4).

Osher and Rudin's shock filter model is very sensitive to noise: the second derivative amplifies noise, and so the location of the real zero-crossings of u_{xx} in (2) is a very difficult task. Several studies have addressed this issue, and various solutions have been suggested. Authors in [14], [20]–[22] have opted to convolve the signal's second derivative with a smoothing Gaussian operator G_σ of standard deviation σ applied to the argument of the shock function of (2)

$$u_t = -sign\,((G_\sigma * u)_{xx})\,|u_x|. \tag{5}$$

The Gaussian operator is not generally sufficient to overcome the noise problems. Indeed, the zero-crossings of $(G_\sigma * u)_{xx}$ depend on the width of the Gaussian support $[-\sigma, +\sigma]$. As shown in Fig. 4, the inflection points of the entity $(G_\sigma * u)_{xx}$ can change according to σ, which makes the identification of inflection points less accurate.

As mentioned in [23], Alvarez and Mazzora proposed a new approach in [14], which combines enhancement and denoising: smoother signal sections are denoised, while edges are enhanced and sharpened. The main idea is to add an anisotropic diffusion term with an adaptive weight to the shock term. This model is written in 2D as follows:

$$I_t = k \cdot I_{\xi\xi} - sign\,(G_\sigma * I_{\eta\eta})\,|\nabla I| \tag{6}$$

where the scalar $k \in [0, 1]$, and ξ is the perpendicular to the gradient direction η; i.e., $\xi = \eta^\perp$.

In [21], Kornprobst *et al.* modified the previous equation to obtain

$$I_t = \alpha_d\,(h_\tau I_{\eta\eta} + I_{\xi\xi}) - \alpha_r\,(1 - h_\tau)\,sign\,(G_\sigma * I_{\eta\eta})\,|\nabla I| \tag{7}$$

where $h_\tau = h_\tau\,(|G_\sigma * \nabla I|) = 1$ if $|G_\sigma * \nabla I| < \tau$ and 0 otherwise. Parameters α_d and α_r are positive scalars. Isotropic diffusion occurs in homogeneous zones ($h_\tau = 1$), whereas the Alvarez and Mazzora shock enhancement behavior occurs in non homogeneous zones ($h_\tau = 0$).

Using a different approach, Coulon and Arridge proposed the following in [20]:

$$I_t = div\,(c\,(\nabla I)) - (1 - c\,(\nabla I))^\alpha\,sign\,(G_\sigma * I_{\eta\eta})\,|\nabla I| \tag{8}$$

where $c\,(\nabla I) = \exp\left(-|\nabla I|^2 / k\right)$. This filter has a similar behavior to the Kornprobst *et al.* model (7), that is, isotropic diffusion in the homogeneous zones where the smoothed image gradient is low, while in zones where the gradient is high, the model behaves as (5).

Gilboa *et al.* [23] proposed a model that relies on complex diffusion:

$$I_t = -\frac{2}{\pi} \arctan\left(a \cdot im\left(\frac{I}{\theta}\right)\right)|\nabla I| + \lambda_1 I_{\eta\eta} + \lambda_2 I_{\xi\xi} \tag{9}$$

where λ_1 is a complex number (r and θ are its *polar* expressions), λ_2 is a scalar, $F(.) = 2/\pi \cdot \arctan(.)$ is the shock function with its argument "$a \cdot im(I/\theta)$," im being the imaginary part of the complex number and a is another scalar which controls the sharpness of the slope at the discontinuity-points.

Finally, Remaki and Cheriet [18] proposed a parametric shock filter to control shock positions, intensity, and propagation velocity. The 2D model is a combination in the $x - y$ directions of the 1D model, as follows:

$$I_t = -a\left(G_\sigma * I^0\right)$$
$$\cdot F\left(\left(G_\sigma * I^0\right)_{\delta\delta}, \left(G_\sigma * I^0\right)_\delta\right) \cdot f_\delta(I)$$
$$\delta = x, y \text{ directions.} \tag{10}$$

In this equation, a, F, and f are functions which control intensity, shock positions, and shock propagation velocity.

Fig. 5 shows a series of enhancements of a synthetic image [Fig. 5(a)] blurred and corrupted with noise [Fig. 5(b)]. The results (image and intensity cross-section profiles in (c)–(h) are shown for the individual shock filters previously described. The image deconvolution changes from filter to filter. The Osher and Rudin [16], [17] shock filter [(4), Fig. 5(c)] does not remove the blur because the detection of inflection points is almost impossible. Images enhanced by filters of Alvarez and Mazzora [14] [(6), Fig. 5(d)], Kornprobst *et al.* [21] [(7), Fig. 5(e)], and Coulon and Arridge [20] [(8), Fig. 5(f)], which all rely on Gaussian smoothing, are fairly similar. The enhanced images obtained using the Gilboa *et al.* [23] filter [(9), Fig. 5(g)] are quite clear, even though no smoothing is used, but the sharpness of edges does not appear optimum. The Remaki and Cheriet [18] results [(10), Fig. 5(h)] are less accurate: sharp discontinuities are created in *ox* and *oy* directions (anisotropic along these two directions), and weak discontinuities are created in other directions of the plane. In conclusion, shock filters are very useful in the piecewise constant segmentations (deconvolution) process. The shock function of the classical deconvolution algorithms can be modified for a new algorithmic behaviors, this lead us to introduce in the next sections an alternative thinning process adapted for the segmentation of SDFT *B*-scan images.

III. SEGMENTATION METHOD

In this section, we describe the segmentation method that consists in two steps: the proposed thinning algorithm and the morphological operators. This method is used to characterize the 2D/3D internal structures of the SDFT by extracting the hyper-echoic structures observed in *B*-scan images and their corresponding fiber fascicle bundles. An analytical and numerical presentation of the proposed thinning algorithm is introduced followed by a detailed description of morphological operations applied to the enhanced images.

A. Thinning Shock Algorithm

To facilitate the understanding of the behavior of the 2D shock filter thinning algorithm on images, its 1D representation, which is easier to analyze analytically, is presented first.
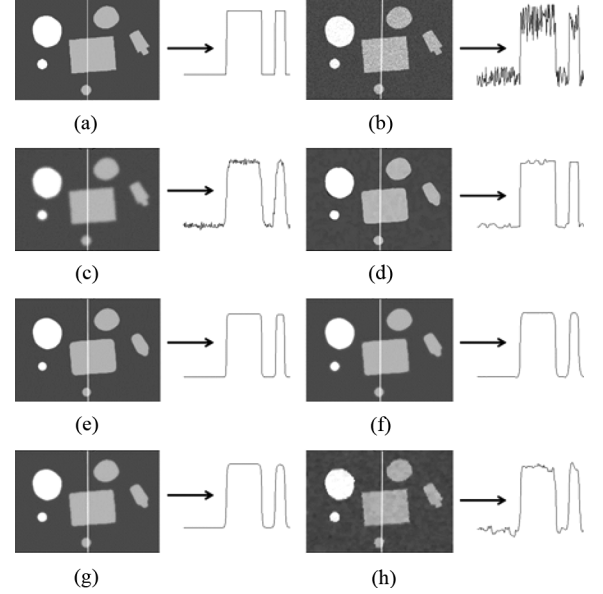

Fig. 5. Mosaic of images and their corresponding intensity profiles, as measured along the arrow seen in each frame. First row (from left): (a) original image, (b) speckle noised image (additive Gaussian noise with a $\mathrm{SNR} = 10$); second row: (c) Rudin shock [16], [17] enhancement, (d) Alvarez & Mazzora [14] enhancement ($k = 0.3$ and $\sigma = 5$); third row: (e) Kornprobst *et al.* [21] enhancement ($\alpha_d = 0.6$, $\alpha_r = 0.4$, $\tau = 0.1$ and $\sigma = 2$), (f) Coulon-Arridge [20] enhancement ($\alpha = 1$, $k = 10$ and $\sigma = 2$); fourth row: (g) Gilboa *et al.* [23] enhancement (λ_1 [$r = 0.7$, $\theta = \pi/6$], $\lambda_2 = 0.3$ and $a = 0.3$); and (h) Remaki and Cheriet [18] enhancement ($\sigma = 2$).

1) One-Dimensional Thinning Shock Algorithm: Our implementation is inspired by the 1D shock filter model proposed in [14], [18] and described as

$$u_t = -F\left(\left(G_\sigma * u^0\right)_{xx}, \left(G_\sigma * u^0\right)_x\right)|\partial_x u| = 0 \text{ in } \Re \times \Re^+ \tag{11}$$

where $u^{0,\sigma} = G_\sigma * u(x, t = 0)$ that is a prior smoothing of the original signal by a Gaussian operator, and the shock function $F(.,.)$ is defined as described in the following sections.

The numerical scheme of the above hyperbolic model (11) is an explicit upwind [18] and is written as follows:

$$\begin{cases} u_i^{n+1} = u_i^n - \frac{\Delta t}{\Delta x}\left(\max\left(0, F_i\right) \cdot \Delta^+ u_i^n \right. \\ \qquad\qquad \left. + \min\left(0, F_i\right) \cdot \Delta^- u_i^n\right) \\ F_i = F\left(\frac{u_{i+1}^{0,\sigma} - 2u_i^{0,\sigma} + u_{i-1}^{0,\sigma}}{\Delta x^2}, \frac{u_i^{0,\sigma} - u_{i-1}^{0,\sigma}}{\Delta x}\right) \\ \Delta^\pm u_i^n = \pm\left(u_{i\pm1}^n - u_i^n\right). \end{cases} \tag{12}$$

The result features depend on the characteristics of the shock function F. In the following, we describe two implementations of F providing either the classical deconvolution operation or the proposed thinning of the signal.

The Shock Function of the Classical Deconvolution Algorithm: For the classical case of deconvolution [14], [18], in which we create sharp discontinuities at inflexion points (i.e., zero-crossings of $u_{xx}^{0,\sigma}$), the function F that satisfies (12) is chosen as follow:

$$F_i^1\left(u_{xx}^{0,\sigma}, u_x^{0,\sigma}\right) = \left(sign\left(u_{xx}^{0,\sigma}\right) \cdot sign\left(u_x^{0,\sigma}\right)\right)_i. \tag{13}$$

x	0		$\pi/2$	π	$3\pi/2$	2π	$5\pi/2$	3π
$Sing(u_x^{0,\sigma})=\cos(x)$		+ 0 -		- 0 +		+ 0 -		
$Sing(u_{xx}^{0,\sigma})=-\sin(x)$	0 -		- 0 +		+ 0 -		-	0
F^1	0 - 0	+ 0	- 0	+ 0	- 0	+ 0		0

- ········· Original signal
- ——— Deconvolued signal

(a)

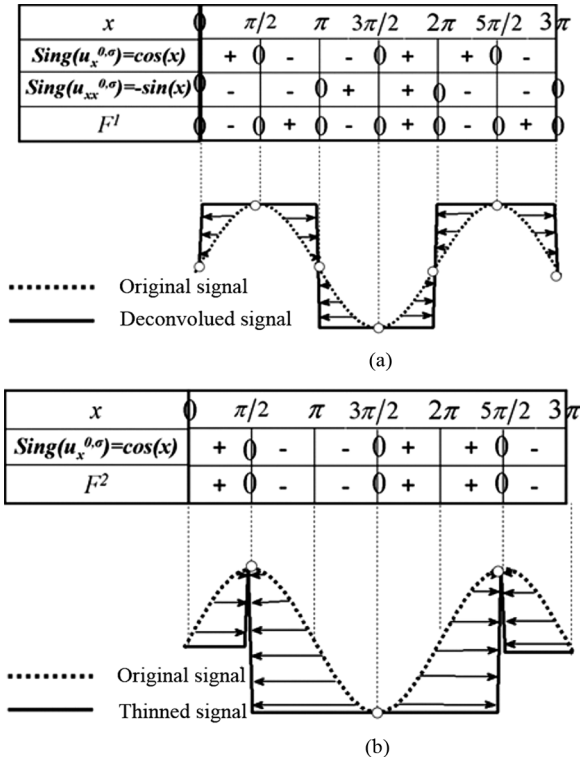| x	0		$\pi/2$	π	$3\pi/2$	2π	$5\pi/2$	3π
$Sing(u_x^{0,\sigma})=\cos(x)$		+ 0 -		- 0 +		+ 0 -		
F^2		+ 0 -		- 0 +		+ 0 -		

- ········· Original signal
- ——— Thinned signal

(b)

Fig. 6. Changes in shock algorithm properties according to the sign of the shock function F. Restoration after 30 iterations of the noise-free curved 1D signal ($u^{0,0} = \sin(x)$) by: (a) the classical 1D deconvolution shock algorithm and (b) our original 1D thinning shock algorithm.
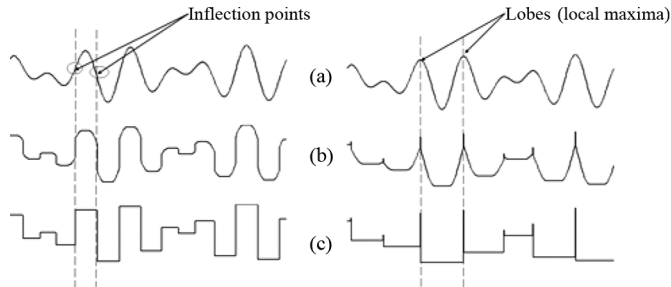
Fig. 7. On left-hand panels, the solution is shown using the classical deconvolution shock algorithm for the initial smoothed signal $u^{0,0} = \sin(5x) + \cos(7x)$. We note discontinuities at the location of the zero-crossings of $u_{xx}^{0,0}$. On right-hand panels, the solution is shown using our original thinning shock algorithm applied on the same signal $u^{0,0}$. The thinning occurs at the location of the local maxima of $u^{0,0}$, (a) original signal, (b) signal sequence at iteration 8 and (c) signal sequence at iteration 30.

Here the subscript 1 is used to define the classical deconvolution process property [14], [18]. Fig. 6(a) is an example showing the evolution of the deconvolution process to create sharp discontinuities in the original signal (the curve signal described by $u^{0,0} = sin(x)$, $x \in [0,3\pi]$) that evolves into a piecewise constant signal. The moving points of the original signal $u^{0,0}$ are governed by the $sign$ of F^1. In the intervals $]\pi/2,\pi[\cup]3\pi/2,2\pi[\cup]5\pi/2,3\pi[$, F^1 is positive and signal points evolve by moving them to the right inducing the creation of jumps at $x = \pi^-$, $2\pi^-$, and $3\pi^-$, while F^1 is negative in the intervals $]0,\pi/2[\cup]\pi,3\pi/2[\cup]2\pi,5\pi/2[$ and signal points evolve by moving them to the left inducing the creation of jumps at $x = 0^+$, π^+, and $2\pi^+$ ("−" and "+" indicate the left

and right values of the central point). We notice that the $sign$ of F^1 is null at points: $x = 0$, $\pi/2$, π, $3\pi/2$, 2π, $5\pi/2$, and 3π in which the signal remains invariant (extreme points).

Shock Function of Our Original Thinning Algorithm: Since our objective is to extract the hyper-echoic structures that are represented by local maxima of the intensity profile of the SDFT *B*-scan image, and inspired by the shock function properties of the classical deconvolution process F^1 [14], [18] described above, the direction of movement of signal points can alternatively be controlled by introducing a new shock function that ensures an erosion process around those local maxima and a dilation elsewhere. The chosen shock function must retain local maxima and minima of the signal, while allowing signal points to move according to the $sign$ of the shock function. A simple choice for the shock function, which can translate these analytical properties into the proposed thinning algorithm, is

$$F_i^2 \left(u_{xx}^{0,\sigma}, u_x^{0,\sigma}\right) = \left(1 \times sign\left(u_x^{0,\sigma}\right)\right)_i = sign\left(u_x^{0,\sigma}\right)_i. \quad (14)$$

The subscript 2 is used here to describe the proposed thinning process property. Fig. 6(b) shows the behavior of this algorithm and moving points of the original signal $u^{0,0}$, which are governed by the $sign$ of the proposed function F^2. Around local maxima of the signal at $x = \pi/2$, F^2 is positive in the interval $]0,\pi/2[$ and signal points evolve to the right of the signal inducing the creation of jumps at $x = \pi/2^-$, while F^2 is negative in the interval $]\pi/2,3\pi/2[$ and signal points evolve to the left of the signal inducing jumps at $x = \pi/2^+$. The $sign$ of F^2 is null and the signal remains invariant at the central point $x = \pi/2$ (local maxima). This process simply reflects erosion around $x = \pi/2$. The algorithm erodes similarly the signal around the local maxima at $x = 5\pi/2$.

Fig. 7 shows the application of the proposed thinning algorithm versus the classical deconvolution method. The input is a 1D noise-free multimodal signal similar to intensity profiles of SDFT *B*-scan images after smoothing by G_σ. Local maxima mimic the hyper-echoic structures corresponding to the interfascicular spaces. The deconvolution algorithm processes the signal by creating a sharp discontinuity that evolves into a piecewise constant signal, while the thinning algorithm erodes signal around local maxima. The thinned process is more practical to our purpose since it thins hyper-echoic structures when applied on SDFT *B*-scan images (as shown later); and it pre-processes them to facilitate their extraction using complementary morphological operations. Both algorithms are based on a stopping criterion on the error between two consecutive signal sequences, with a maximum of 30 iterations.

2) Two-Dimensional Thinning Shock Algorithm: The 2D thinning algorithm based on the same analytical properties as in 1D is described by the following model:

$$\begin{cases} I_t + F\left(\left(G_\sigma * I^0\right)_{\eta\eta}, \left(G_\sigma * I^0\right)_\eta\right)|I_\eta| = 0 \; in \; R^2 \times R^+ \\ I(x,y,t=0) = I^0(x). \end{cases} \quad (15)$$

As in the 1D case, we use the notation $I^{0,\sigma} = G_\sigma * I^0$ for the smoothed initial image. The shock function is not easy to generalize from the 1D model, however, it can be estimated using the structural information contained in such images. Indeed, parallel and linear hyper-echoic structures are formed when the

US wave propagation axis is perpendicular to the interfascicular spaces; in such condition, the gradient vector η is parallel to that axis (η is obviously perpendicular to the hyperechoic structures). Therefore, we assume that the η is simply the y directional derivative of the image (y: vertical direction of the image, x: horizontal direction). The shock function F^2 plays the same role in 2D as in the 1D case, and it is written $F_{i,j}^2 = sign\left(\nabla_y I^{\sigma,0}\right)_{i,j}$. The sign of each column of the matrix F^2 is treated as a 1D signal.

The 2D thinning algorithm scheme then becomes

$$I_{i,j}^{n+1} = I_{i,j}^n - \Delta t \cdot R\left(I_{i,j}^n\right) \tag{16}$$

where

$$\begin{cases} R\left(I_{i,j}^n\right) = \max\left(0, F_{i,j}^2\right)\Delta_y^+\left(I_{i,j}^n\right) \\ \qquad\qquad + \min\left(0, F_{i,j}^2\right)\Delta_y^-\left(I_{i,j}^n\right) \\ F_{i,j}^2 = sign\left(\nabla_y I^{\sigma,0}\right)_{i,j} \\ \Delta_y^\pm I_{i,j}^n = \pm\left(I_{i,j\pm1}^n - I_{i,j}^n\right). \end{cases} \tag{17}$$

B. Complementary Morphological Closing Operations

The segmentation of enhanced B-scan images by 2D mathematical morphological operations was performed to facilitate the extraction of quantitative data on fiber bundles, and also to improve the 2D and 3D visualization of the SDFT internal structures. The mathematical morphological operations proceeded as follows for each enhanced image.

1) Background subtraction using the structuring element "*rolling ball*" with a radius of five pixels.
2) Watershed operation using the validated automatic watershed software (IMAGEJ software, NIH, Bethesda, MD) [24]: an algorithm based on binary thickenings with a structuring element of four connected pixels. The Watershed operation was used to overcome the absence of visible tendon structures parallel to the US beam on B-scan images (see Fig. 2, Fig. 8(e) and (f) as examples of this acoustical phenomenon).

IV. VALIDATION

The proposed imaging technique was first applied on a simulated B-scan image dataset to validate its accuracy and robustness, and on clinical B-scan images to quantify FBD values at various locations along normal SDFTs, and to discriminate normal from injured SDFTs.

A. Simulated B-Scan Image Dataset

B-scan image simulations were performed using the system-based linear model of Bamber and Dickinson [25] at a central frequency of 7.5 MHz. The acoustical impedance of the simulation model was set based on segmented regions representing structural components of the tendon. Collagen and water were identified as the two principal components of a normal tendon [8]: the collagen is mainly located at fiber fascicle bundles and the material within interfascicular spaces and that surrounding the tendon was assumed to be water [26]. A simple thresholding
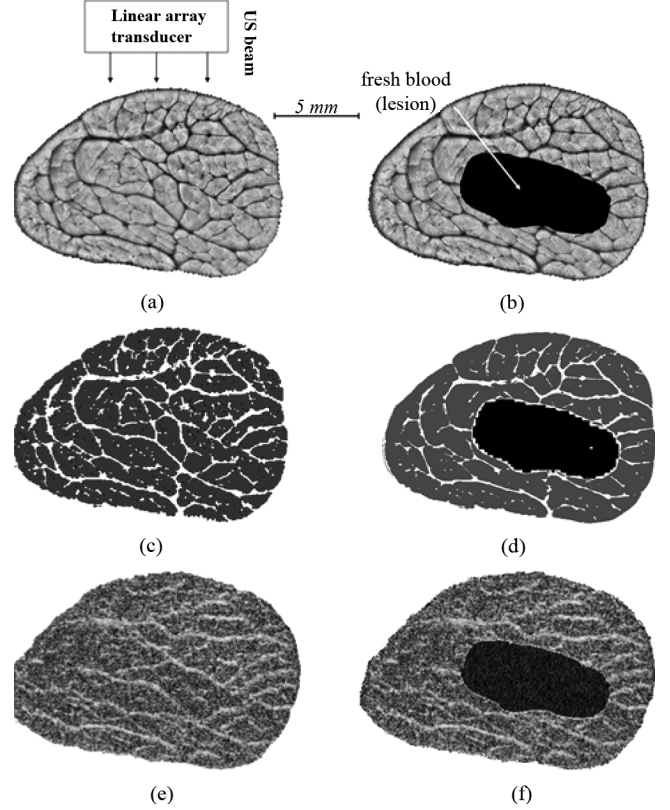

Fig. 8. Simulation results by the Bamber and Dickinson model [25] at a 7.5 MHz central frequency. (a)–(b) macro-photography CSA of a normal and an injured SDFT, (c)–(d) corresponding acoustical impedance map of (a) and (b); and (e)–(f) corresponding simulated B-scan images based on acoustical impedances in (c) and (d).

to segment macro-photography images, as the one presented in Fig. 8(a), provided the realistic acoustical impedance model presented in Fig. 8(c).

Image CSAs where fibers were mimicked as disrupted (pathological cases) were modeled as fresh blood [hemorrhage, dark area in Fig. 8(b) and (d)]. For both normal and injured SDFTs, the assigned acoustical impedances were obtained from [27]–[29] and defined as the scalar product of the compressional wave velocity and the volumetric density of each medium. Postmortem histology slides of two normal SDFTs provided the acoustical impedance map to support the B-scan image simulation [e.g., a normal case in Fig. 8(e), an injured one in Fig. 8(f)]. After fixation of the SDFT tissue with a straight phenolic resin solution, both tendons were cut into 1.3-mm-thick cross sections, regularly spaced using a microtome (Exakt 300 band system, Oklahoma City, OK). CSA aspects of slices were carefully photographed by optical microscopy (Nikon SMZ-U) with a camera (Nikon HFX DX), digitized with a scanner (HP ScanJet 5590, 200 dpi), and stored on a computer [30].

Our B-scan image dataset consist of 238 simulations of two normal SDFT. A standard histomorphometry evaluation [30] was performed to quantify the fiber bundle fascicles from the 238 macro-photography slice references. It consists of an automatic 2D image segmentation followed by a statistical analysis

to deduce the average number of fiber bundle fascicles for each normal tendon.

B. Clinical B-Scan Image Dataset

Clinical *B*-scan images were obtained *in vivo* from eight normal and five injured horses at the *École Vétérinaire d'Alfort*, Maisons-Alfort, Val-de-Marne, France. They were acquired from the equine SDFT in freehand mode scanning with a 7.5-MHz linear array transducer (*SSD-2000-7.5* Aloka, Tokyo, Japan). Tendons were scanned along the loading axis direction (CSA view), from the proximal to the distal part, with a freehand speed displacement of around 1 cm.s^{-1}. The total number of transverse images taken was 150 (± 20) per horse tendon. These were realigned longitudinally by rigid registration [31] to obtain coherent 3D tendon structures.

V. RESULTS

A. Segmentation Results

The segmentation technique was first applied on simulated *B*-scans. Typical US images of a normal and an injured SDFTs are given in Fig. 8(e) and (f), respectively. The challenge of the segmentation method was to recover hyper-echoic structures, on those *B*-scans, to match the gold standard macro-photography references, as depicted in Fig. 8(a) and (b).

The iterative thinning processing of hyper-echoic features was based on a stopping criterion on the error between two consecutive image sequences (with a maximum of 30 iterations). To obtain smoothed symmetrical curved surfaces (2D local maxima) from processed *B*-scans, σ in (15) and (16) was set to 5, which corresponds to the mean thicknesses of hyper-echoic structures on all images (around 10 pixels). Results of Fig. 9 show that the thinning process closely matched the targeted hyper-echoic structures of the intact interfascicular spaces. The thinning process performed erosion around the hyper-echoic structures and dilatation elsewhere [see Fig. 9(a) and (b)]. The region where the lesion is located [hypo-echoic structure in Fig. 9(b)] underwent dilatation similar to an anisotropic diffusion as expected, because of the absence of any bright structures in this region.

The boundaries extracted by the closing morphological operations are projected over the simulated *B*-scan images and over the macro-photography image sources, in Fig. 9(c)–(f), for comparison. As displayed, extracted contours are very realistic for structures perpendicular to the US beam, but coarse in the parallel axis, which is normal and predictable according to the physics of US image formation.

In the case of clinical *B*-scan images [see for examples Fig. 10(a) and (b)], the thinning process produced similar results and also converged towards bright thin lines, which are the targeted interfascicular spaces where fiber bundles were intact [8] [Fig. 10(c) and (d)]. The corresponding 3D surfaces of image close-ups (ROI within boxes) are shown to reveal more effectively thinned structures. The surface of the original selected ROI segment had two hyper-echoic structures degraded by the speckle noise (zoomed panel a). The 3D surfaces following applying our algorithm showed that the
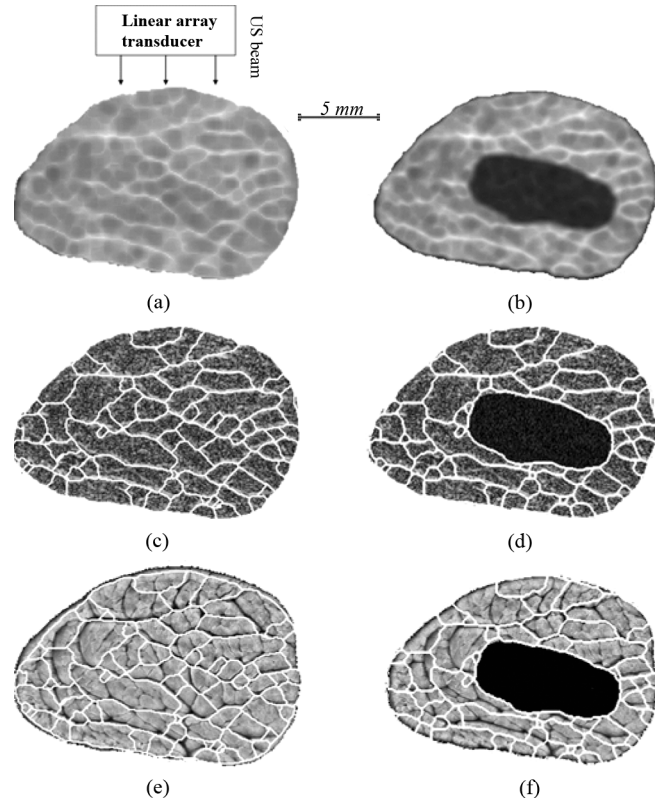

Fig. 9. Segmentation results on simulated *B*-scan images. (a)–(b) Thinned structures of images in Fig. 8(e) and (f), respectively. Superposition of extracted closed structures: (c)–(d) on the simulated *B*-scan images of Fig. 8(e) and (f), and (e)–(f) overlay on the macro-photography images of Fig. 8(a) and (b).

thinning process removed speckle with bright structures becoming thinner (zoomed panel c). Overall, the thinning process successfully converged to bright thin lines corresponding to interfascicular spaces perpendicular to the US beam propagation path through the tissue.

B. Quantification of Fiber Bundle Densities

Fiber bundles were defined as the smallest closed structures in the segmented *B*-scan images [e.g., Fig. 9(c) and (d), Fig. 10(e) and (f)]. In the case of a damaged SDFT, the biggest closed structure defined the injured area [e.g., Fig. 9(d) and Fig. 10(f)]. A spatial rendition of the tendon structure was obtained by stacking series of 2D segmented images in the 3D space.

1) Fiber Bundle Densities in Simulated B-Scan Images: Quantification of FBD has been applied on the simulated *B*-scan image dataset ($n = 238$ images) and mean $\pm$ one standard deviation were 40 (± 8). The gold standard FBD was 42 (± 5); as estimated by histomorphometry [30] on the same specimens (from the 238 macro-photography image references). The agreement between those values shows the effectiveness and accuracy of the proposed segmentation method for the characterization on internal structures of the tendon.

2) Discrimination of in Vivo Normal Versus Injured SDFTs: An additional evaluation was performed on the FBD counted from the whole normal and pathological segmented clinical *B*-scan images. The mean FBD was 51 (± 9) for normal SDFTs and 39 (± 7) for injured ones. In the case of injured SDFTs,
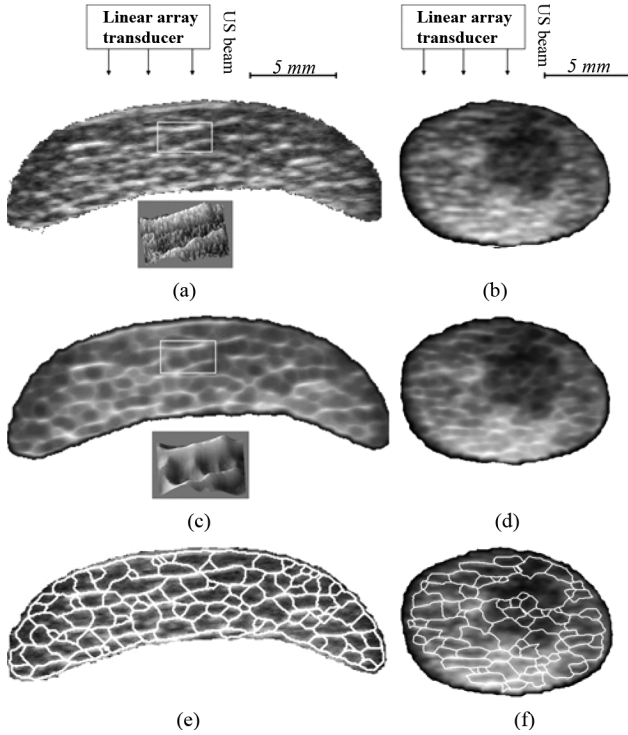
Fig. 10. Segmentation results of clinical *B*-scan images. (a)–(b) *B*-scan images of normal (and corresponding 3D surfaces of the zoomed area of interest) and injured SDFTs, (c)–(d) thinned hyper-echoic structures of panels (a) and (b), and (e)–(f) superposition of extracted closed contours over original images in panels (a) and (b).
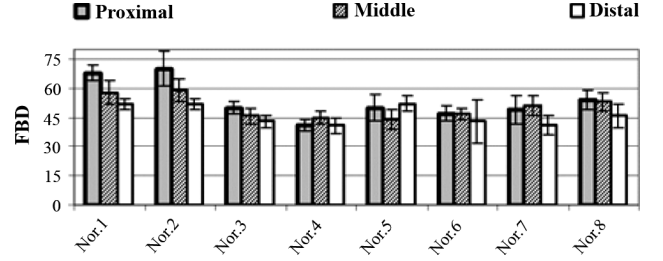

Fig. 11. Fiber bundle density (FBD) at each site of the 8 normal SDFTs.

Fig. 12. Various 3D views of different sites of a healthy SDFT located in the metacarpal region.

only fiber bundles on intact fascicles were considered. The computed FBD value was found to be significantly different between groups, using a student t-test ($p = 0.004$). This difference likely indicates the disruption of some fiber fascicle bundles where lesions have occurred.

3) Fiber Bundle Densities at Three Sites Along the Metacarpal of Normal SDFTs: It is generally accepted that the mechanical strength of the tendon is proportional to its FBD values. From segmented images, the mean FBD calculated for the three sites of the eight normal tendons are presented in Fig. 11. These results show that the mean FBD was highest in five cases out of eight in the proximal part (Nor. 1, 2, 3, 6, and 8), two cases in the middle part (Nor. 4 and 7), and 1 case in the distal part (Nor. 5). Inversely, the mean FBD value was lowest in the distal part in seven cases out of a total of eight (all except Nor. 5). When averaged over the whole dataset, the mean FBD was 54 ($\pm$5) for the proximal, 50 ($\pm$7) for the middle, and 48 ($\pm$8) for the distal segments, respectively (not significantly different based on an analysis of variance with the Bonferroni test for multiple comparisons, $p > 0.05$).

Fig. 12 shows 3D reconstructions of the three parts of a typical normal SDFT: the reconstruction was achieved by stacking successive realigned and segmented images, from which we can appreciate the continuity of 3D structures and the mean FBD. Images of Fig. 12 were taken from our clinical dataset.

VI. SUMMARY AND CONCLUSION

In this study, we have presented an original segmentation method applied on *B*-scan images for the purpose of quanti-

fying internal structures of SDFTs. This method consists of two steps: the first step is the proposed algorithm dedicated to thin hyper-echoic structures observed on the images to facilitate their extraction and the second consists in morphological operations applied on enhanced images to finalize the segmentation of binary closed structures.

The originality of this study is the proposed thinning algorithm adapted to handle *B*-scan ultrasound images. After reviewing analytical properties of existing shock filters and their control parameters [14]–[18], [20], [21], [23], we chose the analytical form of Alvarez and Mazzora [14] and the numerical scheme described in [18] to formulate the proposed shock filter thinning algorithm. Inspired by analytical properties and the *sign* of the shock function of classical deconvolution algorithms [14], [18], we were able to extract hyper-echoic structures "by their thinning" using an adequate shock function. The behavior of the thinning algorithm in the 1D case was related to analytical properties of the chosen function of shock. It is to note that the existence of a unique solution, the stability and convergence of the numerical scheme have already been proven in 1D [14], [18].

The analytical and numerical 2D models of the thinning algorithm, derived from the 1D formulation, are expected to be mathematically and numerically well-posed. The 2D algorithm involves one main parameter: the input standard deviation σ of the Gaussian operator G_σ, which smoothes *B*-scan images. This parameter was pre-estimated based on our whole database, as the mean thickness of hyper-echoic structures and it was fixed to 10 pixels ($2\sigma \approx 10$ pixels). An optimal σ could provide sym-

metrical smoothed curve surfaces of 2D local maxima "similar to the 1D sinusoidal signal" [14], [20]–[22], however, structures whose thicknesses are smaller than 2σ may not be enhanced adequately (large smoothing can cause the loss of these structures).

The effectiveness and robustness of the segmentation method have been tested by extracting the FBD on segmented-simulated *B*-scan images (238 images), obtained from two normal SDFT specimens, which were subject to a standard histomorphometric evaluation (the gold standard) [30]. The agreement between measured and ground truth values confirmed the accuracy of the imaging technique. Also, the statistical analysis on FBD confirmed that our segmentation method could objectively discriminate normal from injured SDFTs. Indeed, the mean FBD of injured SDFTs was smaller $(39\ (\pm 7))$ than that of normal ones $(51\ (\pm 9))$. This clearly reflects the disruption of the thinnest interfascicular spaces and of their corresponding fiber fascicle bundles where lesions occurred [5], [9]. The calculated FBD corroborated values found by a method-based decompression algorithm of *B*-scan images applied by us on the same *B*-scan image dataset [8], where FBD values were found to be $50\ (\pm 11)$ for normal and $40\ (\pm 7)$ for injured tendons.

The FBD statistical analysis of eight normal SDFT cases could not confirm that the proximal and distal sites of the SDFT had highest and lowest mean values. This seems to reflect *in vitro* results [5], showing that mechanical properties of a normal tendon are relatively homogeneous over its entire length. Nevertheless, this disagrees with the observation of a higher occurrence of lesions in the distal metacarpal site [13]. A larger database would certainly be required to confirm or infirm the hypothesis of a link between the fiber bundle density and occurrence of lesions.

ACKNOWLEDGMENT

REFERENCES

[1] N. W. Rantanen, "The use of diagnosis ultrasound in limb disorders of the horse," *Equine Vet J.*, pp. 62–64, 1982.

[2] J. Kastelic, A. Galeski, and E. Baer, "The multicomposite structure of tendon," *Connect Tissue Res.*, vol. 6, pp. 11–23, 1978.

[3] P. M. Webbon, "A post mortem study of equine digital flexor tendons," *Equine Vet J.*, vol. 9, pp. 61–67, 1977.

[4] P. M. Webbon, "A histological study of macroscopically normal equine digital flexor tendons," *Equine Vet J.*, vol. 10, pp. 253–9, 1978.

[5] N. Crevier-Denoix, Y. Ruel, C. Dardillat, H. Jerbi, M. Sanaa, C. Collobert-Laugier, X. Ribot, J. M. Denoix, and P. Pourcelot, "Correlations between mean echogenicity and material properties of normal and diseased equine superficial digital flexor tendons: An in vitro segmental approach," *J. Biomech.*, vol. 38, pp. 2212–20, 2005.

[6] J. M. Denoix and V. Busoni, "Ultrasonographic anatomy of the accessory ligament of the superficial digital flexor tendon in horses," *Equine Vet J.*, vol. 31, pp. 186–91, 1999.

[7] C. Gillis, D. M. Meagher, A. Cloninger, L. Locatelli, and N. Willits, "Ultrasonographic cross-sectional area and mean echogenicity of the superficial and deep digital flexor tendons in 50 trained thoroughbred racehorses," *Am. J. Vet Res.*, vol. 56, pp. 1265–9, 1995.

[8] A. Meghoufel, G. Cloutier, N. Crevier-Denoix, and J. A. de Guise, "Ultrasound B-scan image simulation, segmentation, and analysis of the equine tendon," *Med. Phys.*, vol. 37, pp. 1038–1046, 2010.

[9] C. Martinoli, L. E. Derchi, C. Pastorino, M. Bertolotto, and E. Silvestri, "Analysis of echotexture of tendons with US," *Radiology*, vol. 186, pp. 839–43, 1993.

[10] H. T. M. Van Schie, E. M. Bakker, A. M. Jonker, and P. R. Van Weeren, "Ultrasonographic tissue characterization of equine superficial digital flexor tendons by means of gray level statistics," *Am. J. Vet Res.*, vol. 61, pp. 210–219, 2000.

[11] H. T. M. Van Schie, E. M. Bakker, A. M. Jonker, and P. R. Van Weeren, "Efficacy of computerized discrimination between structure-related and non-structure-related echoes in ultrasonographic images for the quantitative evaluation of the structural integrity of superficial digital flexor tendons in horses," *Am. J. Vet Res.*, vol. 62, pp. 1159–66, 2001.

[12] T. Garcia, W. J. Hornof, and M. F. Insana, "On the ultrasonic properties of tendon," *Ultrasound Med. Biol.*, vol. 29, pp. 1787–1797, 2003.

[13] C. B. O'Sullivan, "Injuries of the flexor tendons: Focus on the superficial digital flexor tendon," *Clin. Tech. An. P*, vol. 6, pp. 189–197, 2007.

[14] L. Alvarez and L. Mazorra, "Signal and image restoration using shock filters and anisotropic diffusion," *SIAM J. Numer. Anal.*, vol. 31, pp. 590–605, 1994.

[15] S. Osher and L. I. Rudin, "Shocks and other nonlinear filtering applied to image processing," *A.G. Tescher (Ed.), Appl. Digital Image Process. XIV, Proc. SPIE*, vol. 1567, pp. 414–431, 1991.

[16] S. J. Osher and L. I. Rudin, "Feature-oriented image enhancement using shock filters," *SIAM J. Numer. Anal.*, vol. 27, pp. 919–940, 1990.

[17] L. I. Rudin, "Images, numerical analysis of singularities and shock filters," Ph.D. dissertation, California Inst. Technol., Pasadena, CA, 1987.

[18] L. Remaki and M. Cheriet, "Numerical schemes of shock filter models for image enhancement and restoration," *J. Math. Imag. Vis.*, pp. 129–143, 2003.

[19] M. Welk, J. Weickert, and I. Galic, "Theoretical foundations for spatially discrete 1-D shock filtering," *Image Vision Comput.*, vol. 25, pp. 455–463, 2007.

[20] O. Coulon and S. R. Arridge, "Dual echo MR image processing using multi-spectral probabilistic diffusion coupled with shock filters," in *Br. Conf. Med. Image Understand. Anal. (MIUA'2000)*, London, U.K., 2000.

[21] P. Komprobst, R. Deriche, and G. Aubert, "Image coupling, restoration and enhancement via PDE's," in *Proc. Int. Conf. Image Process.*, 1997, vol. 2, pp. 458–461.

[22] N. Rougon and F. Preteux, "Controlled anisotropic diffusion," in *Proc. SPIE Conf. Nonlinear Image Process. VI -IS& T/ SPIE Symp. Electron. Imag. Sci. Technol. 95*, San Jose, CA, 1995, vol. 2424.

[23] G. Gilboa, N. Sochen, and Y. Y. Zeevi, "Regularized shock filters and complex diffusion," in *ECCV 2002, LNCS 2350*. New York: Springer-Verlag, 2002, pp. 399–313.

[24] L. Vincent and P. Soille, "Watersheds in digital spaces: An efficient algorithm based on immersion simulations," *IEEE Trans. Pattern Anal.*, vol. 13, pp. 583–598, 1991.

[25] J. C. Bamber and R. J. Dickinson, "Ultrasonic B-scanning: A computer simulation," *Phys. Med. Biol.*, vol. 25, pp. 463–79, 1980.

[26] C. A. Miles, G. A. Fursey, H. L. Birch, and R. D. Young, "Factors affecting the ultrasonic properties of equine digital flexor tendons," *Ultrasound Med. Biol.*, vol. 22, pp. 907–15, 1996.

[27] S. A. Goss and F. Dunn, "Ultrasonics propagation properties of collagen," *Phys. Med. Biol.*, vol. 25, pp. 827–37, 1980.

[28] P. L. Kuo, P. C. Li, and M. L. Li, "Elastic properties of tendon measured by two different approaches," *Ultrasound Med. Biol.*, vol. 27, pp. 1275–84, 2001.

[29] M. W. Moyer and O. Ridge, Table of acoustic velocities and calculated acoustic properties for solids, plastics, epoxies, rubbers, liquids and gases U.S. Dept. Energy, 1997.

[30] G. Leblond, N. Crevier-Denoix, S. Falala, S. Lerouge, and J. A. de Guise, "Three-dimensional characterization of the fascicular architecture of the equine superficial digital flexor tendon," presented at the 6th Int. Conf. Equine Locomotion, Cabourg, Normandy, France, 2008.

[31] P. Thevenaz, U. E. Ruttimann, and M. Unser, "A pyramid approach to subpixel registration based on intensity," *IEEE Trans. Image Process.*, vol. 7, no. 1, pp. 27–41, 1998.